Section 2
PROGRESS IN LASER FUSION

2.A High-Aspect-Ratio Laser-Fusion Targets Driven by 24-Beam UV-Laser Radiation

The compression of spherical, DT fuel pellets to high densities is achieved by depositing laser light on the surface of the target to create a high-temperature, ablating plasma. Many experimental and theoretical studies have established the advantages of short-wavelength laser irradiation for the effective coupling of laser energy into a high-density collisional plasma[1-5] (without the generation of copious suprathermal electrons[5-6]) and for the generation of high ablation pressures[7] sufficient to drive an efficient compression on a low isentrope. From simple heuristic arguments,[8] and from the predictions of two-dimensional (2-D) hydrodynamic simulations,[9] implosion uniformity of spherical-shell targets to high final-core densities under direct multibeam laser irradiation will be maintained only for modest initial shell-aspect-ratios $[(R/\Delta R)_o]$ under a high degree of illumination uniformity.

Low-aspect-ratio targets will be used in future high-density experiments on OMEGA. However, the first set of UV implosions were performed with high-aspect-ratio targets because they were predicted to produce the relatively high neutron yields needed to checkout diagnostics, which measure the fuel and shell areal densities. Computer simulations show that the high yield is produced, in part, by a strong shock that propagates through the fuel and preheats it. (However, the shock preheat also limits the amount of fuel compression.) The calculations also show that the initially high aspect ratio is, in fact, substantially reduced early in the implosion due to expansion of the shell from radiative preheat, making the target less vulnerable to disruption by

the Rayleigh-Taylor instability. The targets used were relatively large, resulting in low peak intensities ($< 2 \times 10^{14}$ W/cm^2); this minimizes the generation of fast electrons from parametric processes,[10] simplifying the modeling of thermal energy transport within the target.

The experiments discussed in this report were made with large-diameter, large-aspect-ratio [$(R/\Delta R)_0 \sim 300$], DT-filled glass microballoons. A large number of plasma, x-ray, and nuclear diagnostics were deployed to characterize the coronal plasma, the hydrodynamics of the implosion, and the final compressed core conditions. These included a time-resolving x-ray streak camera[11] and a transmission grating,[12] x-ray spectroscopy and photography,[13] and neutron time-of-flight spectrometry.[14] The measurement of the fuel and shell areal densities was made using fuel ion (knock-on) spectrometry[15] and neutron activation,[16] respectively. Simulations of these experiments were made with the one-dimensional (1-D) hydrodynamic code, *LILAC*,[17] which includes inhibited thermal transport, LTE radiation physics, and laser energy deposition via a ray-tracing algorithm in the underdense plasma. Neutron yields in these experiments were as high as 2×10^{11}, the highest so far reported for any laser-fusion experiments.[18]

Hydrodynamic simulations of these thin-walled, large-diameter glass microballoon targets give considerable insight into the characteristics of the implosion. The predicted behavior of a characteristic target is shown in Figs. 24.3 and 24.4. The target was a glass microballoon, ~ 750 μm in diameter, containing 10 atm of DT gas, with a wall thickness of ~ 2 μm. It was irradiated with 2 kJ of 351-nm radiation in 700 ps (average intensity $\sim 1.83 \times 10^{14}$ W/cm^2). Although $(R/\Delta R)_0 = 185$, it can be seen from Fig. 24.3(b) that the effective-aspect ratio decreases rapidly during the acceleration phase of the implosion and has decreased to ~ 20 at the half-radius point. Figures 24.3(c) and 24.3(d) show that the majority of the energy is absorbed during the first half of the implosion; 83% of the total absorbed energy is deposited by the time the maximum implosion velocity (5×10^7 cm/s at the fuel-glass interface) is reached. The peak intensity in the absorption region, specifically at the critical density surface ($n_c \sim 10^{22}$ cm^{-3}), never exceeds 1.0×10^{14} W/cm^2 [Fig. 24.3(d)], which is below the values expected for the onset of parametric instabilities producing suprathermal electrons. The predicted 1-D time histories for neutron production, DT ion temperature and density, and fuel and shell areal density are shown in Figs. 24.4(a) through 24.4(d), respectively. The neutron generation in Fig. 24.4(a) commences on the convergence of the first shock, which propagates with a velocity greater than 5×10^7 cm/sec. The average DT ion temperature and density rise to maximum values of ~ 6 keV and ~ 0.7g/cm^3, respectively [Fig. 24.4(b)], at the time of maximum compression. At this point in the implosion, the fuel and shell areal densities have risen sharply to the maximum values indicated in Figs. 24.4(c) and 24.4(d). The 1-D neutron yield for this simulation is 2.4×10^{12}.

The actual implosion experiments used DT-filled (10 atm), 700- to 800-μm-diameter glass microballoon targets with wall thickness in the

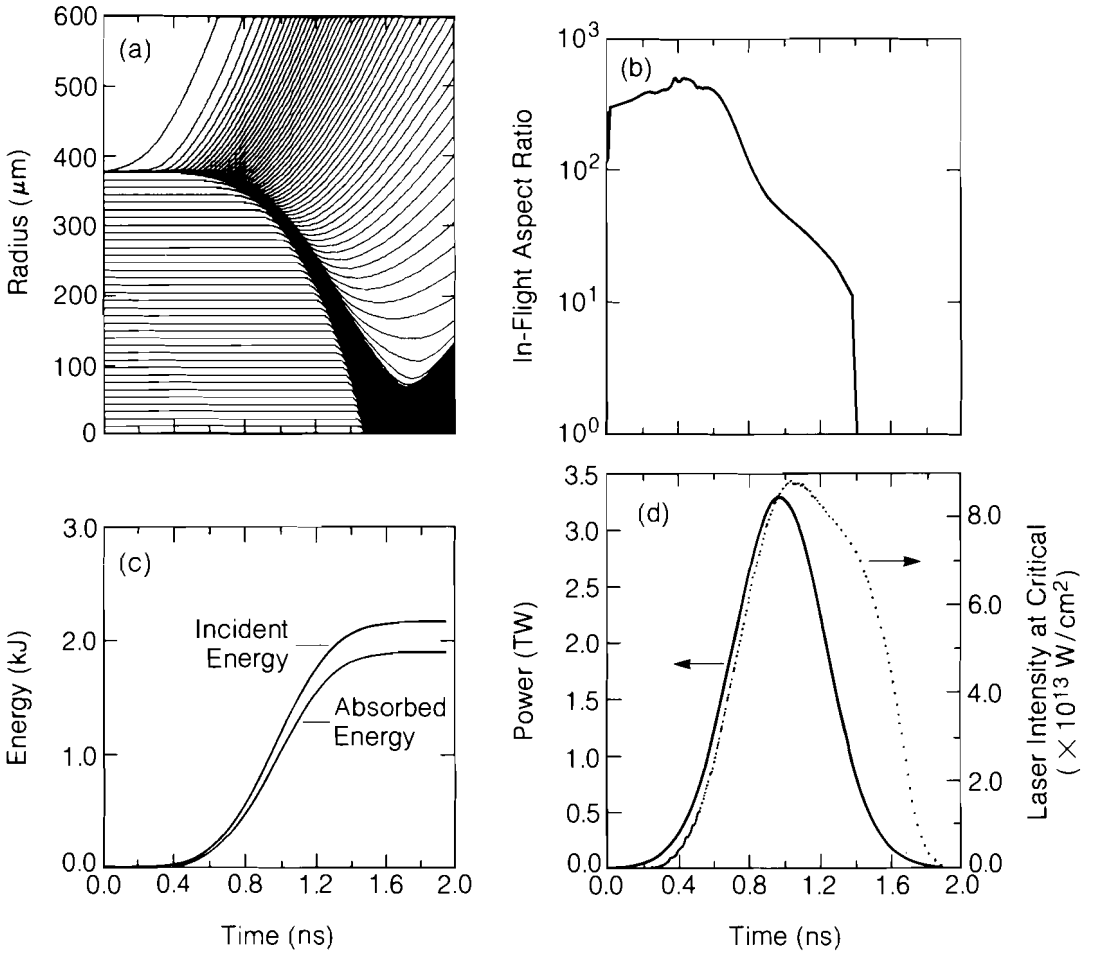

Fig. 23.3
One-dimensional LILAC *simulations of the implosion of a DT-filled (10 atm), 700-μm-diameter, 2-μm-wall glass microballoon irradiated with a 2-kJ, 700-ps pulse of 351-nm laser light:*
(a) radius-time (R-t) plot of the Lagrangian elements;
(b) in-flight-aspect ratio;
(c) time-integrated laser absorption; and
(d) intensity at the critical surface as a function of time during the implosion.

range of 1.3–2.1 μm, and were performed using the newly up-converted 24-beam OMEGA laser system.[18] The beams were focused on target with 600-mm-focal-length (f/3.7), single-lens optics. Up to 2.4 kJ of 351-nm laser radiation was delivered to the target in a 700-ps pulse (FWHM), with a 3% beam energy variance. The individual beams had lateral and axial positional accuracies of 10 and 50 μm, respectively. They were focused to various positions beyond the target center, in order to vary the degree of beam overlap and illumination uniformity. From a characterization of the intensity distribution in the

target plane, a minimum level of illumination nonuniformity of 16% rms was estimated for a focus of 10 target radii (F = 10R) beyond the target center. These targets, irradiated with an average intensity of 2×10^{14} W/cm^2, had an estimated peak-to-valley intensity variation of 60%. The overall absorption, measured with an array of differential plasma calorimeters, was 80%, and, to within 5%, was invariant for focal positions between F = 4R to 9R. Measurements of the continuum x-ray emission spectrum indicated, as with earlier 6-beam experiments on solid spherical targets,[5] that $< 10^{-4}$ of the absorbed energy was coupled to collisionless suprathermal electrons.

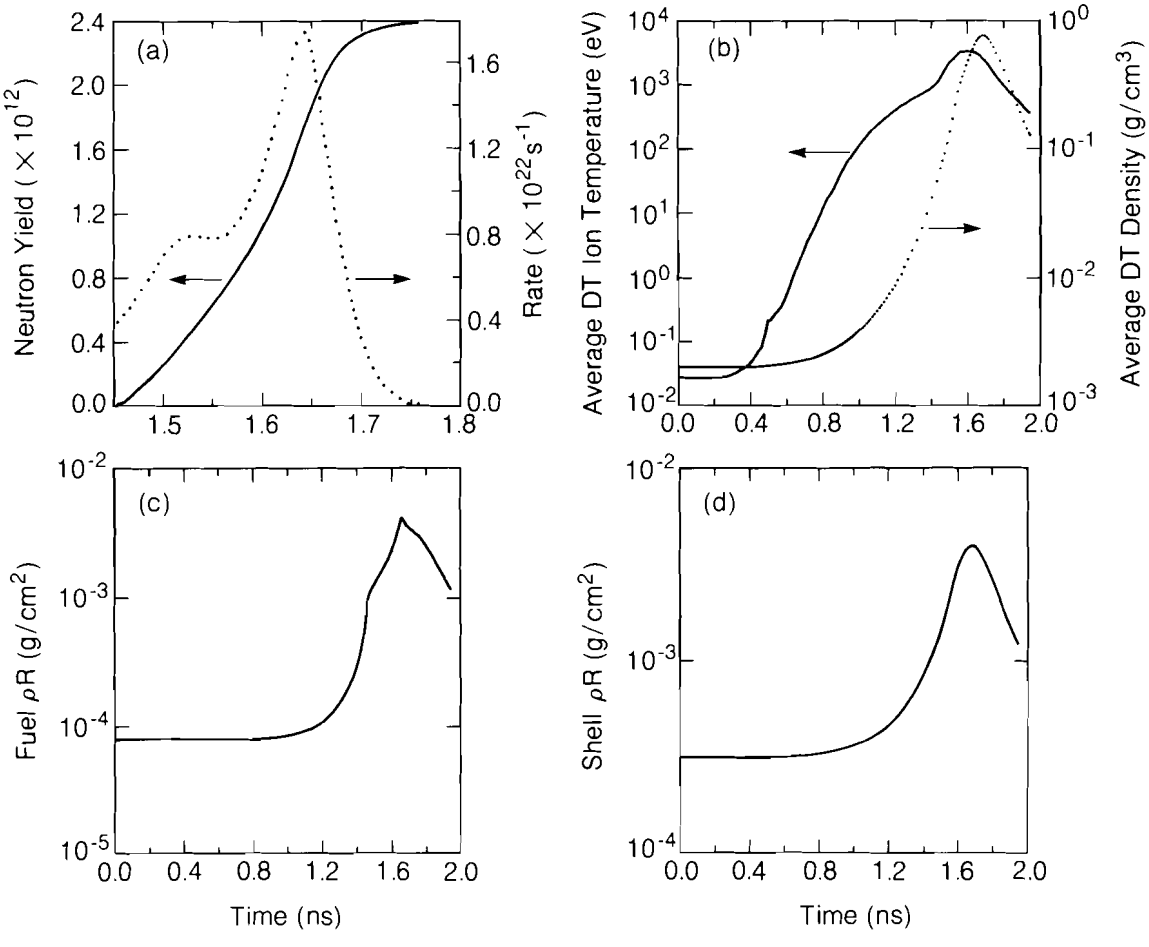

Fig. 24.4
Calculated time histories of target conditions during the implosion:
(a) integrated neutron yield and neutron production rate;
(b) mass-averaged fuel-ion temperature and fuel density;
(c) average fuel areal density; and
(d) average shell areal density.

Several diagnostic systems were deployed to determine the hydrodynamics and final core conditions of the imploding target. Time-integrated x-ray photography, with either a pinhole camera (x-ray energy E ~ 2 keV) or a Kirkpatrick-Baez microscope (E ~ 4 keV), spatially resolved the x-ray emission from the imploding shell. Figure 24.5(a) shows a plot of contours of a constant film x-ray exposure as determined from such an x-ray micrograph. The image contains a central region of emission, ~120 μm in diameter. This feature is the result of x-ray emission from the inside wall of the shell, which is heated in the final stages of the implosion — initially by the outward-going reflected shock in the compressed fuel, and finally by electron thermal conduction from the hot fuel to the shell. The azimuthal average of this image about the implosion center [Fig. 24.5(b)] indicates that the average radius of the emitting region was ~50 μm at the time of peak emission. The corresponding simulation of the x-ray micrograph by the hydrodynamic code *LILAC* [Fig. 24.5(b)] shows an emission region of approximately the same size produced by the stagnating shell.

Measurements of the fuel and shell areal densities were made using knock-on fuel-ion spectrometry[15] and neutron activation of ^{28}Si, respectively. These techniques probe the compressed target conditions

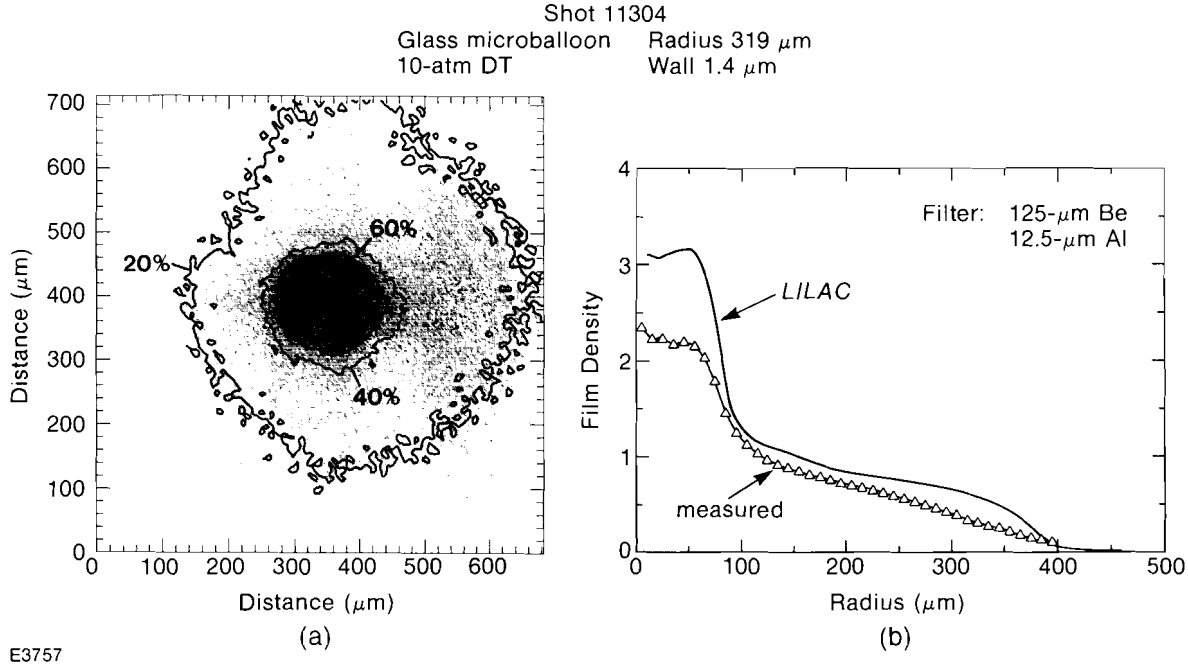

Fig. 24.5
Details of a 4-keV micrograph of x-ray emission from the target.
(a) 2-D contour plot of the x-ray intensity overlaid on a density-shaded reduction of the x-ray micrograph;
(b) azimuthally averaged x-ray intensity deduced from (a), compared to the predicted x-ray intensity from the hydrodynamic code LILAC.

at the time of maximum neutron generation. The shell ρR was measured using the number of $^{28}Si(n,p)\ ^{28}Al$ reactions (cross section $\sigma = 0.25b$) induced in the imploded glass shell, by detecting[19] the coincident 1.78-MeV γ-ray and 2.86-MeV β-particle decays of ^{28}Al (half-life 2.25 min). A small fraction ($\eta_c \sim 0.8\%$) of these particles was collected by a thin (50-μm) Ti cone collector and rapidly extracted from the target chamber with an automatic extraction and collection system.[20] The number of activations N_c^* initially counted is related to the neutron yield (Y_n) and the average shell area density $<\rho\Delta R>$ by $N_c^* = k_c Y_n <\rho\Delta R>$, where k_c includes η_c, σ, and factors accounting for the counting duration and the delay between activation and onset of counting. To exceed the threshold level of measurement in these experiments, defined as 10 recorded counts in 5 min (background level ~ 1 count/1.2 min), the required $Y_n <\rho\Delta R>$ product must be $\gtrsim 10^7$ neutrons g/cm^2.

The average fuel $<\rho R>$ was estimated from the number of deuterons and tritons scattered by the 14.6-MeV DT neutrons in the compressed fuel. A fraction of these was detected by thin (100-μm) CR-39 nuclear track detectors deployed in Ta-filtered, gas-filled cells (to reduce background tracks); the detectors subtend a maximum solid angle of $\sim 1\%$. The number of coincident tracks[15] (N_T^*) on both sides of the etched CR-39, produced by the scattered deuterons and tritons, is directly related to Y_n and to the average fuel ρR by $N_t^* \sim k_t Y_n <\rho R>$, where k_t includes the collection fraction and the fraction of the total scattered ion distribution recorded by the track detector. For $<\rho R>$ values less than $\sim 4 \times 10^{-3}$ gm/cm^2, the latter is constant, as the thin imploded shell will not distort the spectrum of scattered deuterons and tritons.[21] (With several of these detectors deployed around the target, inferences about the uniformity of the compressed core could be made.) For a counts/background ratio of 10, and an ion collection fraction above 1% of the total solid angle, the required $Y_n <\rho R>$ product is $\sim 10^6$ neutrons g/cm^2.

The measured neutron yield as a function of the focus parameter for two-diameter ranges of thin-wall glass microballoon targets is shown in Fig. 24.6. The maximum yield (2×10^{11}) was found for $F = 4R$, a focus condition for which the 24, f/3.7 beams of OMEGA are contiguously focused on the target surface. This yield, however, is considerably lower (by a factor of 20) than that predicted [see Fig. 24.4(a)]. Some insight into the behavior of the target during the final stages of the implosion, when neutrons are produced, can be obtained by comparing the measured values of the neutron yield and the fuel and shell areal densities with those predicted by *LILAC* (Fig. 24.4 and Table 24.I). The measured values of Y_n, ρR, and $\rho\Delta R$ correspond to the predicted values of these parameters at a time of ~ 50 ps before the final stagnation, corresponding approximately to the time that the first compression wave reaches the center of the target and rebounds against the inside wall of the shell. After this time, it is possible that hydrodynamic instabilities disrupt the shell during the final stage of the implosion. The interpretation of the implosion results is at present speculative, and requires further analysis of the experimental data.

- Maximum neutron yield generated for contiguous beam irradiation of target

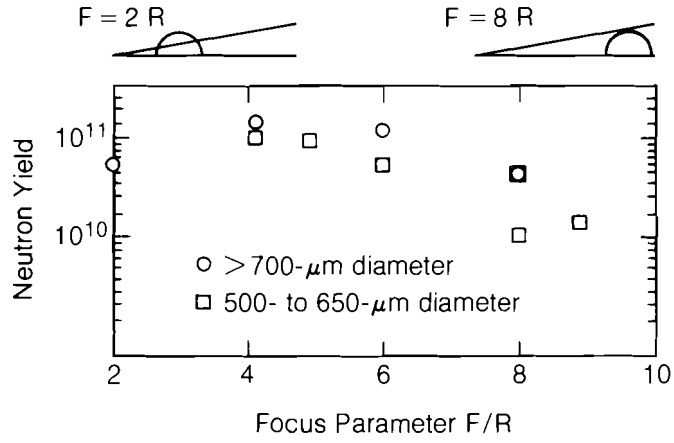

E3627

Fig. 24.6
Neutron yield versus laser-beam focus (in units of target radii behind the target center). Tangential focus corresponds to ~7.5.

Characteristic Experimental and Theoretically Predicted Compressed Core Parameters (Shot 11200)

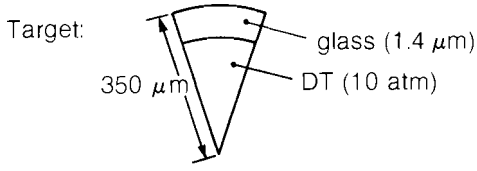

Laser: Energy = 2.2 kJ
Intensity = 2.3×10^{14} W/cm^2

	SIMULATION		EXPERIMENT	
	Total	First Compression		(No. of Counts)
Neutron Yield	1.2×10^{12}	1.5×10^{10}	2.7×10^{10}	($\sim 10^4$)
Fuel ρR	2.5×10^{-3} g/cm^2	9.1×10^{-4} g/cm^2	5.8×10^{-4} g/cm^2 $\pm 0.6 \times 10^{-4}$ g/cm^2	(120)
Shell ρR	3.2×10^{-3} g/cm^2	1.2×10^{-3} g/cm^2	1.1×10^{-3} g/cm^2 $\pm 0.1 \times 10^{-3}$ g/cm^2	(130)

E3756

Table 24.I.
Characteristic experimental and theoretically predicted compressed core parameters (shot 11200).

ACKNOWLEDGMENT

This work was supported by the U.S. Department of Energy Office of Inertial Fusion under agreement number DE-FC08-85DP40200 and by the Laser Fusion Feasibility Project at the Laboratory for Laser Energetics which has the following sponsors: Empire State Electric Energy Research Corporation, General Electric Company, New York State Energy Research and Development Authority, Northeast Utilities Service Company, Ontario Hydro, Southern California Edison Company, The Standard Oil Company, and University of Rochester. Such support does not imply endorsement of the content by any of the above parties.

REFERENCES

1. D. C. Slater *et al.*, *Phys. Rev. Lett.* **46**, 1199 (1981).
2. W. C. Mead *et al.*, *Phys. Rev. Lett.* **47**, 1289 (1981).
3. W. Seka *et al.*, *Opt. Commun.* **40**, 437 (1982).
4. C. Garban-Labaune *et al.*, *Phys. Rev. Lett.* **48**, 1018 (1982).
5. M. C. Richardson *et al.*, *Phys. Rev. Lett.* **54**, 1656 (1985).
6. R. L. Keck *et al.*, *Phys. Fluids* **27**, 2762, (1984).
7. B. Yaakobi *et al.*, *J. Appl. Phys.* **57**, 4354 (1985).
8. J. Nuckolls, L. Wood, A. Thiesson, and I. Zimmerman, *Nature* **239**, 139 (1972).
9. LLE Review **23**, 125 (1985).
10. A. Simon, R. W. Short, E. A. Williams, and T. Dewandre, *Phys. Fluids* **26**, 3107 (1983).
11. B. L. Henke and P. A. Jaanimagi, *Bull. Am. Phys. Soc.* **29**, 1388 (1984).
12. M. C. Richardson, R. S. Marjoribanks, S. A. Letzring, J. M. Forsyth, and D. M. Villeneuve, *IEEE Quant. Electron.* **QE-19**, 1861 (1983).
13. M. C. Richardson, S. A. Letzring, W. Friedman, and G. Gregory, *High-Speed Photography, Videography, and Photonics* (SPIE, Bellingham, WA, 1983), Vol. 427, p. 91.
14. S. A. Letzring, G. Pien, L. M. Goldman, M. C. Richardson, and J. M. Soures, *Bull. Am. Phys. Soc.* (to be published).
15. S. Kacenjar, S. Skupsky, A. Entenberg, L. Goldman, and M. C. Richardson, *Phys. Rev. Lett.* **49**, 463 (1982); S. Kacenjar, L. M. Goldman, A. Entenberg, and S. Skupsky, *J. Appl. Phys.* **56**, 2027 (1984).
16. E. M. Campbell *et al.*, *J. Appl. Phys.* **51**, 6062 (1980).
17. University of Rochester, LLE Report No. 16 (1976).
18. M. C. Richardson *et al.*, *Proceedings of 1985 Conference on Lasers and Electro-Optics* (IEEE, New York, 1985), p. 234.
19. S. M. Lane, E. M. Campbell, and C. Bennett, *Appl. Phys. Lett.* **37**, 600 (1980).
20. The collection efficiency of the Ti cone collectors, which subtended ~2% of the fuel solid angle, was estimated independently by measuring the ^{28}Si decay from activated empty glass microballoons.[16]
21. S. Skupsky and S. Kacenjar, *J. Appl. Phys.* **52**, 2608 (1981).